

Super-Resolution Algorithm for Deep Undercooling Melt Image Based on Adaptive Mixed Sample



Yuehai Wang, Ze Su, Shiming Cui, Yuying Ma, Yang Yang*

School of Information Science and Technology, North China University of Technology,
No. 5, Jinyuanzhuang Road, Shijingshan District, Beijing, China
{wangyuehai, yangy}@ncut.edu.cn, {su_ze28, cuishiming10, mayuying27}@163.com

Received 7 January 2019; Revised 1 July 2019; Accepted 28 August 2019

Abstract. The limitation of resolution seriously affects the study of deep undercooling melt. Nowadays, the existing image super-resolution (SR) methods cannot restore the high-resolution (HR) image from a low-resolution (LR) image, and is not suitable for reconstructing the texture details of the deep undercooling melt. To solve these problems, we propose a method based on adaptive mixed sample and low-rank matrix decomposition optimization (AMS-LMDO) for single-image SR. Unlike other SR methods, we make a full use of the external and internal sample libraries to extract the complementary prior knowledge. Comparing with other individual sample libraries, the experimental results prove our method is more effective. Moreover, we also apply low-rank matrix decomposition to optimize reconstructed-HR image, which carried with sparse and uncorrelated errors and erroneous information. The simulation results show that compared with the current popular methods, the proposed method can not only restore the general images, but also recover the inherent high frequency details of the deep undercooling melt.

Keywords: deep undercooling melt, low-rank matrix decomposition, mixed sample library, super-resolution

1 Introduction

With the continuous achievement of human civilization, synthesizing and producing new substances, instead of researching and utilizing the existing materials, become the bottleneck of technological development. Researchers recently found that under specified conditions even if the temperature drops below the freezing point, several certain melts will still stay in a liquid state when (1) itself has no crystal nucleus; (2) it is in an environment where nothing is in contact with it. This state is called deep undercooling.

New properties will appear when the deep undercooling melt turns into the solidified state. The researchers used electrostatic suspension and vacuum drop tubes to simulate this environment, and shot deep undercooling melt for free-fall until it stepped into solidified state with high-speed cameras. Meanwhile, they studied the properties of the material with the obtained images. For example, Gao et al. [1] observed the properties of the Nd-Fe-Co-B alloy droplets in the deep undercooling state. Luo and Chen [2], Kamal et al. [3] discovered that under microgravity conditions, deep undercooling material will reveal vital material properties, which are very beneficial for discovering new materials. However, according to the Zou et al. [4], in the vacuum drop tube simulation experiment, in order to fully solidify the melt, the falling time of object should be more than 3.2 seconds, thus the required length of the drop tube is not less than 50 meters. In this situation, and maximum speed of the melt drop is about 31.26 m/s. Due to the limitation of the high-speed camera, the spatial resolution of the captured image is quite low, and the texture is blurry, which greatly restrict the research of the new properties of deep undercooling melt. To solve this problem, Zou et al. [4] employed an image super-resolution reconstruction algorithm

* Corresponding Author

to obtain a better deep undercooling melt image, which contained more texture information and edge information. Since then, SR becomes the most effective solution to solve above problems. However, till now, there are still few SR algorithms applying for deep undercooling melt.

Since SR is an extremely ill-posed problem, the restored image is not unique. For the purpose of reducing the multi-possible HR images, a lot of researchers [5-8] has shown that prior knowledge can be used to constrain the result of the reconstruction. In summary, according to the difference in the source of prior knowledge, image SR can be divided into two types: (1) external-sample-library (ESL) based SR methods; (2) internal-sample-library (ISL) based SR methods.

ESL-based SR methods use a large number of external samples for dictionary training to obtain sufficient prior knowledge, and encode the mapping between LR image and the corresponding HR image. And then, the LR image can be decoded into HR image according to the former coding principle. The basis of encoding and decoding is the sparse representation dictionary. Tropp et al. [9] pointed that the quality of dictionary depends on whether it can sparsely represent signals, the more sparse the representation, the more accurate the reconstructed signal. Because the ESL contains a large number of HR images and various high-frequency details, the learned dictionary can represent images very sparsely, so ESL-based SR method is preferred by researchers. But this method has its own limitations: it does not guarantee that any input LR image can be restored better to its original image, especially when the LR image is greatly different from the samples from ESL, the reconstruction may contains a lot of error information, which would result in a severe distortion between the reconstruct image and the original image.

For these problems, researchers have proposed an ISL-based SR method to utilize the self-similarity of the image: numerous identical structures exist in the same or different size image patches [10]. These repetitive structures can be used as prior knowledge to constrain the HR image with smaller difference to the original image. Compared with the ESL-based method, the information extracted from the ISL is highly interrelated with the input image, which greatly improves the accuracy of reconstruction. However, this method also shows the limitation because of its assumption that the image has self-similarity. In the case that the input image has no obvious repeated small patches, the prior knowledge provided by the self-similarity is insufficient, and thus the reconstructed image produces perceptual errors.

Like coins have two sides, both of methods have their own limitations. ESL provides more high-frequency information, but the reconstruction effect is not ideal if the ESL is much different from the test images; Although the ISL can provide more accurate prior knowledge by the image self-similarity, when the LR image itself has fewer similar structures, artificial marks (e.g., sawtooth and smoothness) may appear in the reconstructed image. Currently, image processing techniques based on both ISL and ESL are mostly used for image denoising [11]. Mosseri et al. [12] first concluded that for better denoising, some image patches should be extracted from ESL, while the others have better effects on ISL. This inspires us whether we can find a way to combine the advantages of ISL and ESL to restore the images.

In this paper, we proposed an improved method to reconstruct the deep undercooling melt. We named the proposed algorithm adaptive mixed sample and low-rank matrix decomposition optimization (AMS-LMDO). The proposed AMS-LMDO has several appealing properties. First, our method can adaptively select ISL and ESL to extract more instrumental prior knowledge; Second, our method further optimizes the reconstructed image and removes their error message. The general flow of the method is shown in Fig. 1. The red part is: (1) generating an image pyramid from the input LR image, (2) utilizing the image self-similarity and the nearest neighbor match to generate a set of HR images. The green part is: (1) generating two coupled dictionaries according to the dictionary learning, (2) using our proposed adaptive mixed sample library selection model (AMSLSM) to generate a HR image. The blue part is: (1) extracting the high-low frequency information of the HR image, (2) combining them to generate a group of HR images with error information, (3) using the low-rank matrix decomposition optimization (LMDO) to remove the error message in the reconstructed images, (4) obtaining the final more accurate HR image.

The contributions of this paper are mainly in three aspects:

(1) The Adaptive Mixed Sample Library Selection Model (AMSLSM) is proposed for single-image SR, which can not only organize the external and internal sample libraries (mixed sample library) effectively, but also choose a more appropriate method to reconstruct image patches adaptively.

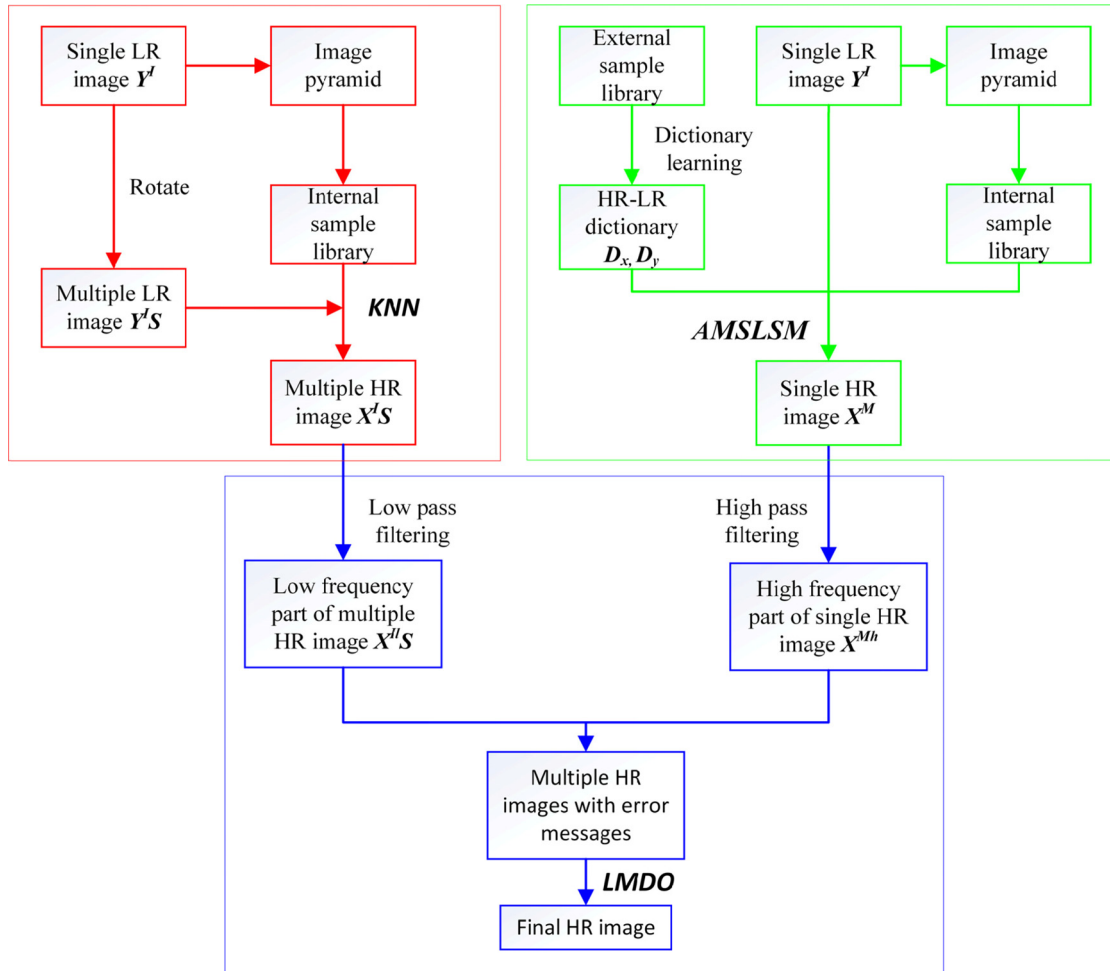


Fig. 1. Overview of the proposed method

(2) Low-rank matrix decomposition optimization (LMDO) is used to optimize a set of error-contained HR images, especially for deep undercooling melt images. This method can effectively work with the complementary information provided by the mixed sample library, to remove error information and generate a more perceptual HR image.

(3) Proposed method is in a leading position for reconstructing the deep undercooling melt, which can well restore their texture information and edge information. In the meantime, our method is also competitive with other popular algorithms on the public datasets.

The remainder of this paper is organized follows: Section 2 reviews the related work and various popular SR methods. Section 3 presents the proposed method in detail, including establishment of ISL, dictionary learning, sparse reconstruction, AMSLSM and LMDO. Section 4 demonstrates the effectiveness of the method by comparing it with state-of-the-art SR techniques. The conclusion is given in Sec. 5.

2 Related Works

According to the background of the deep undercooling melt, we choose sample-based method to learn the prior knowledge. As mentioned in the previous section, the common sample-based learning method can be divided into ESL-based and ISL-based. The ESL-based method falls into Markov field [13-14], sparse representation and dictionary learning [15-16], improved dictionary learning [17-20], and anchored neighborhood regression [21-22] etc. The ISL-based method mainly focuses on image self-similarity (e.g., [10, 23-24]). Table 1 supplies the comparison between the above methods and ours. In the next part, we will briefly explain ESL-based and ISL-based method respectively.

Table 1. Comparison between the related work and our method

method	Library selection	Core theory	optimize after restoration
Freeman et al. [13]	ESL	Markov random field	
Zhang et al. [14]	ESL	Markov random field	
Yang et al. [15-16]	ESL	sparse representation dictionary learning	
Wang et al. [17]	ESL	improved dictionary learning	
Zeyde et al. [18]	ESL	improved dictionary learning	
Dong et al. [19-20]	ESL	improved dictionary learning	
ANR/A ⁺	ESL	anchored neighborhood regression	
Glasner et al. [10]	ISL	image self-similarity theory	
Zhu et al. [23]	ISL	image self-similarity theory improved K-SVD	
Yang et al. [24]	ISL	image self-similarity theory group sparse constraints	
AMS-LMDO (our method)	Mixed sample library	sparse representation improved dictionary learning image self-similarity theory low-rank matrix decomposition	Use LMDO to further improve the reconstructed image

In the field of SR, a huge amount of research has focused on using ESL to learn prior knowledge. Among them, Freeman et al. [13] proposed a Markov-random-field-based method to reconstruct similar images from candidate pools, but if the relevant images are missing from the database, the reconstruction results will be very poor. Zhang et al. [14] proposed a high-order Markov random field model as a priori knowledge, and then predicted HR images according to the Markov chain Monte Carlo sampling algorithm. Yang et al. [15-16] proposed a SR method based on sparse representation and dictionary learning. By establishing a training sample library, obtained the dictionaries that can sparsely express HR and LR image blocks respectively. Then combined with the theory of compressed sensing to complete the SR reconstruction, finally achieved good results. Wang et al. [17] proposed a new mapping learning method, which simultaneously learns dictionary pairs and mapping functions. Among them, dictionary pairs reveal features of inter-image domains, while the mapping functions illustrate the essential relationship between LR images and HR images. Zeyde et al. [18] proposed a new dictionary learning algorithm based on K singular value decomposition (K-SVD) method, and performed SR reconstruction based on orthogonal matching pursuit (OMP) method. Dong et al. [19-20] used adaptive selection means to build a sub-dictionary of low-resolution image blocks, and introduced two regular terms: (1) local autoregression; (2) local self-similarity, to further improve reconstruction efficiency. Timofte et al. [21-22] combined the sparse representation with the anchored neighborhood regression to speed up the single-image-super-resolution (SISR) reconstruction and named them ANR and A⁺, respectively. The ESL-based methods are widely used because ESL can provide very clear high-frequency details, but the method does not guarantee that the original high-resolution image can be restored well for any input image. Especially dealing with special texture-detail or edge-information contained images (e.g., deep undercooling melt), the learnt dictionary cannot accurately represent the image. More seriously, the noise is added during reconstruction, which will result in the HR image too smooth and artificial.

On the other hand, ISL-based methods use image self-similarity theory to enhance the prior knowledge to decrease the quantity of the possible reconstructed images. For example, Glasner et al. [10] used the above facts and combined with the multi-frame image SR method to perform single-image SR. Zhu et al. [23] proposed a sample self-similarity algorithm using the improved K-SVD method and directly used OMP to generate HR images. Yang et al. [24] combined image self-similarity theory with image pyramid to generate HR-LR image patches. Further, they used group sparse constraints as prior knowledge to solve the ill-posed problem in SR.

So far, there is little work involved in using the mixed dictionary for image restoration, and most of the work applied to image denoising. Recently, Wang et al. [25] proposed a joint learning method based on mixed sample library for image reconstruction. They attempted to compare the Signal-to-noise ratio (SNR) of the two reconstructed images to determine whether the internal dictionary or the external dictionary is used. Wang et al. [26] first added the low-rank matrix decomposition to the image restoration method, and a good reconstruction effect was obtained. These aspects inspired us to find an

improved SR method. On the contrary, our proposed method is based on mixed sample library to extract more accurate information. It not only has more obvious reconstruction effects on ordinary images, but also is more suitable for deep undercooling melt.

3 Method

The method proposed in this paper is divided into three parts: image reconstruction based on ISL, image reconstruction based on mixed sample library, and low-rank matrix decomposition optimization (LMDO). The image reconstruction based on mixed sample library includes dictionary learning, sparse reconstruction and adaptive mixed sample library selection model. To facilitate the following reading, we provide the Table 2 to list the symbols used in the equations.

Table 2. Symbols used for our equations in Section 3

symbols	Representation	symbols	Representation
Y^l	LR image	F_{LR}	feature matrix
$\{y_i^l\}_{i=1}^n$	patches extracted from Y^l	X^E	ESL-based HR image
Y^D	down-sampled image	Ω	bicubic interpolation
Y^{Dl}	low-frequency domain of Y^D	φ	sparse weight
$\{y_j^{Dl}\}_{j=1}^m$	patches extracted from Y^{Dl}	r	total number of sparse patches
$\omega_{i,j}$	reconstruction weight	$E_e(\alpha_i)$	ESL-based reconstruction error
$Z(i)$	ordinary constant	$E_i(x_i^l)$	ISL-based reconstruction error
h	filter degree parameter	x, y, w, z	empirical parameters
$\{x_i^s\}_{i=1}^n$	image patches	λ	patch-based adaptive weight
D	overcomplete dictionary	p	hyperparameter
α	sparse coefficient	\bar{X}	HR image with error information
λ	sparsity constant	X^{ll}	low-frequency part based on the ISL
τ	sparsity threshold of the coefficient	X^{Mh}	high-frequency part based on the mixed sample library
x_i	patches extracted from HR image	L	low-rank matrix
y_i^l	patches extracted from LR image	S	sparse matrix
F	mapping function	γ	sparsity weight
Ψ	PCA projection matrix	\hat{X}	The final reconstructed image

3.1 Image Reconstruction Based on Internal Sample Library

Recently, Wang et al. [26] proposed an improved method based on nearest neighbor matching to acquire HR and LR patches pairs. However, the reference only amplified the input images, so the searching space of similar patches is small. In order to expand the search range, we not only up-sampled the input images, but also down-sampled them, and performed similar processing according to the method in the reference, after that we obtained more similar patches of the LR images.

Fig. 2 shows our improved method, where the cyan frame is the extracted patches, the pink frame is the corresponding low frequency part, the blue frame is the corresponding high frequency part, the dotted arrow indicates that the two parts are similar, and the line arrow indicates the addition of the two parts. Giving an input LR image Y^l , up-sampling it by different magnification factors, and we named it Y^U . At the same time, a high-pass filter is used to decompose the input LR image Y^l into low-frequency domain Y^{ll} and high-frequency domain Y^{lh} respectively. Next, patches $\{y_i^U\}_{i=1}^n$ are extracted from the up-sampled image Y^U , which serve as low frequency parts of the HR patches $\{x_i^l\}_{i=1}^n$. Then we search for extracted-patches-similar $\{y_j^{ll}\}_{j=1}^m$ from the patches y_i^{ll} , which belong to the low-frequency domain Y^{ll} , and the corresponding high frequency patches $\{y_j^{lh}\}_{j=1}^m$ are regarded as the high frequency part of HR patches $\{x_i^l\}_{i=1}^n$. In this way, the HR image X^l can be obtained by adding high and low frequency patches. Next, the input image is down-sampled to Y^D by different zoom factors, and a high-pass filter is used to

decompose Y^D into low frequency domain Y^{Dl} and high frequency domain Y^{Dh} respectively. Then, patches $\{y_i^l\}_{i=1}^n$ are extracted from the input LR image Y^l , and these patches serve as low frequency parts of the HR patches $\{x_i^l\}_{i=1}^n$. We search for extracted-patches-similar $\{y_j^{Dl}\}_{j=1}^m$ from the patches y_j^{Dl} , which belong to the low frequency domain Y^{Dl} , and the corresponding high frequency patches $\{y_j^{Dh}\}_{j=1}^m$ are regarded as the high frequency portion of the HR patches $\{x_i^l\}_{i=1}^n$. Similarly, a HR image X^l based on the ISL is obtained.

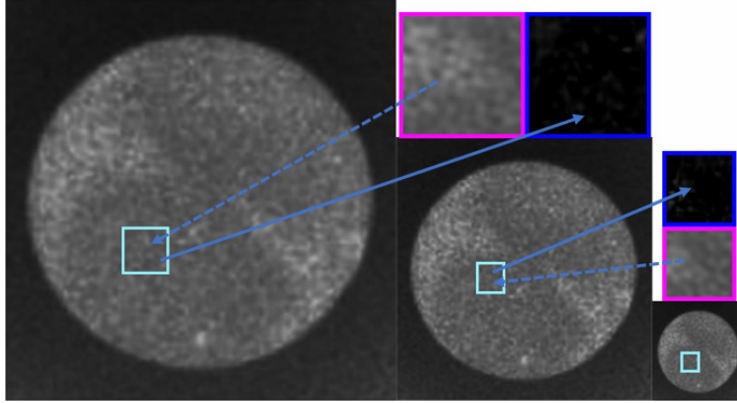


Fig. 2. Establishment of an internal sample library

In order to maximize the generalization ability of the ISL, different nearest neighbor search thresholds k is applied during the experiment, managing to search more similar image patches. However, experiments have shown that when the number of similar patches in the image is small, if the value of k is arbitrarily increased, the selected patches will be much more different from each other, which result in a very large distortion between the restored image and the original image. To extend the searching space again, an affine transformation matrix is estimated in the down-sampled patches to match the target patches and their neighboring patches. By doing like this, a flexible range of k can be got to ensure the diversity and accuracy of the image. According to the method in Buades et al. [27], after the value of k is determined, the reconstruction weight $\omega_{i,j}$ of each matching patch can be calculated by solving the equation

$$\omega_{i,j} = \frac{1}{z(i)} \exp\left(-\frac{\|y_i^l - y_j^{Dl}\|_2^2}{h_2}\right), \quad (1)$$

where $Z(i)$ is the ordinary constant and the parameter h is a filter degree parameter. Next, L2 norm (Euclidean distance) is used as the calculation standard for patch matching. The benefit of this procedure is that it sensitive to rotation. After plenty of experiments, we found that the results obtained by different angle are also different, so the input image is rotated by 8 angles (0, 45, 90, 135, 180, 225, 270, 315) to searched for similar patches in the image. Finally, we can get $k*8$ restored HR images X^lS based on ISL.

3.2 Image Reconstruction Based on Mixed Sample Library

Reconstruction methods based on mixed sample library are different from ISL-based. Wang et al. [25] stated that some of the reconstructed HR patches is similar to ESL, while the others prefer ISL. If LR image can easily achieve the relative information from ESL, the restoration will be very accurate only based on ESL, and vice versa. If the LR image contains many repetitive patches at the same or different scales, then the ISL will play a crucial role during the reconstruction because of image self-similarity theory. Therefore, how to combine the ISL and ESL to complement each other's advantages becomes the key to generate HR images. Our proposed Adaptive Mixed Sample Library Selection Model (AMSLSM) can adaptively decide which library should be use, according to the expression effect of different patches

in the corresponding ISL and ESL. This section mainly explains the image SR method based on the ESL and the proposed AMSLSM, the image SR method based on ISL is described in Sec. 3.1.

Dictionary learning. Dictionary learning plays a vital role in the process of sparse reconstruction. Researchers have proposed various dictionary learning methods. Originally, Aharon et al. [28] designed a pair of HR and LR dictionaries for image reconstruction. Yang et al. [29] proposed a method for image SR based on group dictionary learning. Dong et al. [21] used a series of PCA methods and adaptive selection optimization sub-dictionary methods to obtain corresponding HR images. Zhang et al. [30] used SVD to learn adaptive dictionaries, which corresponding to each set of input images, to reconstruct HR images. Dictionary learning usually attempt to find an overcomplete dictionary $D \in R^{a \times b}$ ($a < b$), so that as many image patches $\{x_i^l\}_{i=1}^n \in R^a$ as possible can be sparsely represented under this dictionary. In other words, the dictionary is satisfied with

$$\begin{aligned} & \arg \min_{D, \{\alpha_i\}_{i=1}^n} \sum_{i=1}^n \|x_i^S - D \alpha_i\|_2^2 + \lambda \|\alpha_i\|_1, \\ & \text{s.t. } \|D(:, k)\|_2 \leq 1, \forall k \in \{1, 2, \dots, K\}, \|\alpha_i\| \leq \tau, \end{aligned} \quad (2)$$

where $D(:, k)$ is the k th column of dictionary D , α_i is the sparse coefficient of x_i^S , λ is the sparsity constant of the control representation coefficient, and τ is the sparsity threshold of the coefficient. Different from the standard dictionary learning method, we used the joint sparse coding to solve the dictionary learning problem according to [29].

We define the input LR image as Y^l , apply y_i^l and D_y as its patches and sparse dictionary respectively. The corresponding HR image is X , and x_i , D_x are its patches and sparse dictionary respectively. We assume that there is a mapping relationship F satisfies

$$x_i = F(y_i^l). \quad (3)$$

Therefore, if y_i^l is known, and F can be found, the original HR image can be restored. The key to find F is to generate a pair of dictionaries D_x and D_y to satisfy with

$$\begin{aligned} & \arg \min_{D_x, D_y, \{\alpha_i\}_{i=1}^n} \sum_{i=1}^n \|x_i - D_x \alpha_i\|_2^2 + \|y_i^l - D_y \alpha_i\|_2^2 + \lambda \|\alpha_i\|_1, \\ & \text{s.t. } \|D_x \& D_y(:, k)\|_2 \leq 1, \forall k \in \{1, 2, \dots, K\}, \|\alpha_i\| \leq \tau. \end{aligned} \quad (4)$$

The equation shows that the generated dictionaries D_x and D_y should sparsely represent HR and LR image patches, and their representation coefficients should be as similar as possible. In order to be more concise, there are the definitions

$$\tilde{x}_i = \begin{bmatrix} x_i \\ y_i^l \end{bmatrix}, \tilde{D} = \begin{bmatrix} D_x \\ D_y \end{bmatrix}. \quad (5)$$

Therefore, Eq.(4) is converted to the standard sparse reconstruction problem with Eq.(5):

$$\begin{aligned} & \arg \min_{\tilde{D}, \{\alpha_i\}_{i=1}^n} \sum_{i=1}^n \|\tilde{x}_i - \tilde{D} \alpha_i\|_2^2 + \lambda \|\alpha_i\|_1, \\ & \text{s.t. } \|\tilde{D}(:, k)\|_2 \leq 1, \forall k \in \{1, 2, \dots, K\}, \|\alpha_i\| \leq \tau. \end{aligned} \quad (6)$$

By solving Eq.(6), the corresponding HR and LR dictionary pairs can be obtained.

Different from directly using the original pixel values, we first extracted the sample features from the original HR and LR image patches, and then remove the average of the sample pixels. The advantage of doing this is to reduce the amount of calculations. In the mapping process of HR and LR images, the average value of image patches can be well preserved. In this way, adding the mean value to the pixel value after calculating the result does not affect the reconstruction effect. Since the low-frequency information of the LR image patches is most relevant to the missing high-frequency information, the gradient features of the LR images are extracted according to the method in [13]. When the features of the HR and LR patches are extracted, we find that the HR and LR image pairs are closely related to a

more complex relationship than the linear relationship. The process of finding HR patches by LR patches is mathematically a pseudo-inverse process, similar to compressed sensing.

In order to train dictionaries pairs, we sample from an ESL, which contains a large number of clear HR images $\{X_j^S\}_{j=1}^N$, and obtain many HR patches $\{x_i^S\}_{i=1}^n$. For each HR image patch, we blur, down-sample, and bicubic-interpolate to get the same size LR image as the original image. We define these images as $\{Y_j^S\}_{j=1}^N$. From these image pairs $\{X_j^S, Y_j^S\}_{j=1}^N$. We use the former solutions to sample n pairs HR and LR patches of size $p \times p$, and then extract their features. After that, training data $\{x_i^S, y_i^S\}_{i=1}^n$ is obtained. In order to prevent the sampled data from being too similar, those patches with little difference are removed, this operation also prevents the reconstructed image having more error information. After getting the training dataset, the dictionary pair is trained according to algorithm 1. Briefly explain a few parts. The step 2 can have different methods for initializing dictionary pairs: (1) initializing dictionary pairs using conventional sparse encoding methods; (2) randomly initializing dictionary pairs using mathematical methods; the step 6, $\eta(t)$ is the step size of the stochastic gradient descent, and the shrinkage rate is $1/t$; In order to meet the constraint of the dictionary, each column of $D_y^{(n)}$ is normalized using L2 norm in step 7.

Algorithm 1.

- (1) **Input**: training patch pairs $\{x_i^S, y_i^S\}_{i=1}^n$ and HR-LR dictionaries size.
 - (2) **Initial**: initialize $D_x^{(0)}$ and $D_y^{(0)}$, $t=1$, $n=1$.
 - (3) **Repeat**
 - a. **For** $i = 1, 2, \dots, N$ **do**
 1. Compute gradient $\beta = dL(D_x^{(n)}, D_y^{(n)}, x_i^S, y_i^S) / dD_y$.
 2. Update $D_y^{(n)} = D_y^{(n)} - \eta(t) * \beta$.
 3. Project the columns of $D_y^{(n)}$ onto the unit ball.
 4. $t = t + 1$.
 - b. **End for**
 - c. Update $D_y^{(n+1)} = D_y^{(n)}$.
 - d. Update $D_x^{(n+1)}$.
 - e. $n = n + 1$.
 - (4) **Until convergence**.
 - (5) **Output**: HR-LR dictionaries $D_x^{(n)}$ and $D_y^{(n)}$
-

Sparse reconstruction. Given the input LR image Y^l , up-sampling is performed by bicubic interpolation operation to zoom in the image to the desired size. Then the gradient and Laplacian features are extracted along their lateral and longitudinal directions. The feature patches are respectively extracted from the four feature images and combined into the feature matrix F_{LR} . Since the higher dimension of the feature matrix enlarge the subsequent calculations, we apply the Principal Component Analysis (PCA) projection matrix Ψ to reduce the dimension of the feature matrix F_{LR} . The sparse coefficient a of the feature matrix can be calculate by OMP [31] and the LR image dictionary, which obtained in Sec.3.2.1. The equation is

$$\arg \min_{\alpha} \|\Psi^T F_{LR} - D_y a\|_F^2 \quad \text{s.t.} \quad \|a_{\rho}\|_0 \leq \tau \quad \forall \rho, \quad (7)$$

Where a_{ρ} is the ρ th column of a . We define R_{ξ} as the patch extraction operation, and $R_{\xi} X$ is the ξ th patch of X . Therefore, reconstructed HR image can be obtained according to the conclusion in [15], which HR and LR images share the similar sparse representation within the respective dictionaries. The solving formula is

$$X^E = \Omega Y^l + \varphi \left(\sum_{\xi=1}^r R_{\xi}^T R_{\xi} \right)^{-1} \sum_{\xi=1}^r R_{\xi}^T D_x a, \quad (8)$$

where X^E is a HR image reconstructed based on an ESL, Ω represents bicubic interpolation, parameter φ represents sparse weight, and r is the total number of sparse patches.

Adaptive mixed sample library selection model. It is well known that high frequency information is the key to SR. In order to obtain the high-frequency portion of the original HR image X , Adaptive Mixed Sample Library Selection Model (AMSLSM) is built to adaptively select more efficient representations of the patches. On this basis, inspired by Dong et al. [20], given an input LR image patch y_0^l , the least squares regression (LSR) is used to turn the reconstruction into mathematical problem, and the L2 norm regular term is used to overcome this extreme ill-posed multi-solution problem. The sparse representation coefficients are also determined by OMP to obtain a reconstructed HR image. Next, we will explain in detail how to adaptively select the most efficient patches.

Mosseri et al. [12] demonstrated the preference of image reconstruction for ESL and ISL based on SNR criteria. However, this method does not fully consider the similarity between images. Thus, we define the function E , which weights and sums the SNR and SSIM values of the image by two empirical parameters, and the result is used as the reconstruction error. The ESL-based reconstruction error method is defined as the error information between the sparse representation image and the input LR image:

$$E_e(\alpha_i) = x * SNR(\mathbf{D}_y \alpha_i, y_i^l) + y * SSIM(\mathbf{D}_y \alpha_i, y_i^l). \quad (9)$$

At the same time, ISL-based reconstruction error method is defined as the error information between the matching image and the input LR image:

$$E_i(x_i^l) = w * SNR(y_i^l, x_i^l) + z * SSIM(y_i^l, x_i^l). \quad (10)$$

Since the ISL-based SR mainly relied on the repetitive patches of the LR image itself, the parameters of the two kind of error information are usually inconsistent.

The values of these two kinds of error information are usually on the same order of magnitude, which is also in line with the fact that the internal and external sample library have a common performance in the similar regions for image reconstruction. However, there are some image patches, which indeed cause a large difference in the value of the two kind of error information. For example, some image patches are easy to find similar images in the external image, and other image patches are repeated in the image itself. So, the patch-based adaptive weights need to be defined as:

$$\Lambda(\alpha_i, x_i^l) = \exp(p * [E_e(\alpha_i) - E_i(x_i^l)]), \quad (11)$$

where p is a hyperparameter. When the external error message turns larger, the corresponding weight drops rapidly to ensure the internal self-similarity dominate, and vice versa.

The reconstructed HR image X^M based on the mixed sample library can be obtained by the above procedure.

3.3 Low-rank Matrix Decomposition Optimization

According to Wang et al. [26], the image features reconstructed based on the ISL are dense, while the images reconstructed based on the ESL contain more feature details, and the distribution is sparse. The images reconstructed by the method described in Sec. 3.2 obviously provide more high-frequency detail. Therefore, a low-pass filter is used to process the reconstructed image based on the ISL, and obtain the low-frequency part X^l . The high-pass filter is used to process the reconstructed image based on the mixed sample library to obtain the high-frequency part X^{Mh} . Combining the high frequency and low frequency parts, a number of HR images

$$\bar{X} = X^l + X^{Mh}, \quad (12)$$

are obtained with many error messages. Since these HR images are very similar, they share the same low-dimensional structure, and the remaining error information is sparse and independent. The resulting HR images are vectorized into a matrix \bar{X} , where the relevant parts can be transformed into a same low-dimensional subspace. Meanwhile, the remaining uncorrelated parts of the original space are error information. In other words, the final HR image to be reconstructed can be approximated as a low-rank matrix. Therefore, the image optimization problem is regarded as a dimension reduction problem, the LMDO is used to decompose \bar{X} into a low-rank matrix and a sparse matrix. The reason for using LMDO

to solve this problem is that it has been proved that the low-rank related parts can be extracted from one matrix, while the rest are sparse non-correlated parts.

In order to get the low-rank part, we define

$$\bar{X} = L + S, \quad (13)$$

where L is a low-rank matrix and S is a sparse matrix. The more sparse S , the more accurate we get the L . Therefore, this problem is now converted to how to decompose the most sparse S , and there is a the mathematical expression:

$$\min_{L,S} \|L\|_* + \gamma \|S\|_1, \text{ s.t. } L+S = \bar{X}, \text{ rank}(L) \leq \delta. \quad (14)$$

Here $\|L\|_*$ is the kernel norm of L , $\|S\|_1$ is the L_1 norm of S , and γ is the sparsity weight to adjust S . Due to the huge computational complexity of the SVD when the matrices are large, and the problem is extreme ill-posed, we use the alternating projection method (APM) to solve these problems. This method is similar to the solution proposed in [26], by fixing one of the unknowns to solve another. The mathematical expressions are as:

$$L_t = \arg \min_{\text{rank}(L) \leq \delta} \|\bar{X} - L - S_{t-1}\|_F^2, \quad (15)$$

$$S_t = \arg \min_{\text{card}(S) \leq \tau} \|\bar{X} - L_{t-1} - S\|_F^2, \quad (16)$$

where $\text{card}(\cdot)$ is the number of non-zero elements in the matrix. Thus, after the low-rank matrix decomposition, many HR images are obtained, and finally the average of all those HR images is taken as the final reconstructed image \hat{X} .

We summarize the proposed method in Algorithm 2.

Algorithm 2.

- (1) **Input**: LR image Y^l , magnification factor, training patch pairs $\{x_i^s, y_i^s\}_{i=1}^n$, HR-LR dictionary size, sparse threshold τ , preference parameters x, y, w and z , PCA projection matrix Ψ , iteration number, extracted patch size, overlapping size.
 - (2) Build an image pyramid Y^D, Y^l, Y^U .
 - (3) Rotate the input image and extract patches.
 - (4) **For** each HR patch $\{y_i^U\}_{i=1}^n$ **do**
 - a. Decompose LR patches into $\{y_j^{lh}\}_{j=1}^m, \{y_j^{ll}\}_{j=1}^m$.
 - b. search y_j^{ll} in $\{y_j^{lh}\}_{j=1}^m$. $\triangleright y_j^{ll}$ similar to y_j^U .
 - c. $\omega_{i,j} \leftarrow \frac{1}{Z(i)} \exp(-\frac{\|y_i^l - y_j^{ll}\|_2^2}{h^2})$.
 - d. $x_i^l \leftarrow \omega_i * y_i^U + \omega_j * y_j^{lh}$.
 - (5) **End for**
 - (6) prepare $D_x^{(n)}$ and $D_y^{(n)}$. \triangleright calculate from Algorithm 1.
 - (7) Prepare F_{LR} .
 - (8) PCA dimension reduction for feature matrix.
 - (9) $\alpha \leftarrow \arg \min_{\alpha} \|\Psi^T F_{LR} - D_y \alpha\|_F^2, \text{ s.t. } \|\alpha_{\rho}\|_0 \leq \tau \forall_{\rho}$.
 - (10) $x_i^E \leftarrow QY^l + \varphi \left(\sum_{\xi=1}^r R_{\xi}^T R_{\xi} \right)^{-1} \sum_{\xi=1}^r R_{\xi}^T D_x \alpha$.
 - (11) **For** each LR input patch y_j^l **do**
 - a. $E_e(\alpha_i) \leftarrow x * \text{SNR}(D_y \alpha_i, y_i^l) + y * \text{SSIM}(D_y \alpha_i, y_i^l)$.
 - b. $E_i(x_i^l) \leftarrow w * \text{SNR}(y_i^l, x_i^l) + z * \text{SSIM}(y_i^l, x_i^l)$.
 - c. $\Lambda(\alpha_i, x_i^l) \leftarrow \exp(p * [E_e(\alpha_i) - E_i(x_i^l)])$.
-

-
- d. HR image x_i^M . \triangleright based on mixed sample library.
- (12) **End for**
- (13) Using high-pass filtering to process HR image x^M to get X^{Mh} .
- (14) Using low-pass filtering to process HR image x^l to get x^{ll} .
- (15) $\bar{X} \leftarrow x^{ll} + X^{Mh}$.
- (16) $\hat{X} \leftarrow \min_{L,S} \|L\|_* + \gamma \|S\|_1$, s.t. $L+S=\hat{X}$, $\text{rank}(L) \leq \delta$.
- (17) **Output:** The final HR image \hat{X} .
-

4 Experimental Results and Analysis

In order to verify the effectiveness of our algorithm, the relevant comparison experiments will be carried out in the following two aspects: (1) reconstruction contrast of ordinary images; (2) reconstruction contrast of deep undercooling melt. At the same time, in each experiment we performed 2 times and 3 times down-sampling on the test images respectively, after the same reconstruction processing, the experimental results proved the robust of our method.

We used MATLAB R2016b to build an experimental environment on a computer (Inter i7 dual-core 3.4GHz processor and 8GB memory) and conducted a series of simulation experiments. After that, we compared proposed AMS-LMDO with the popular methods and our AMSLSM:

- BIC- bicubic interpolation method
- YangSR - the sparse representation method used by Yang et al. [15]
- ZeydeSR - the sparse coding method used by Zeyde et al. [18]
- TimofteSR - the regression method used by Timofte et al. [14]
- HuangSR - the self-exemplars method used by Huang et al. [32]
- KimSR - the very deep convolutional networks method used by Kim et al. [33]
- AMSLSM - our proposed adaptive mixed sample library selection model

The implementations are all from the public available codes provided by the authors, and all image are down-sampled using the same bicubic kernel.

In dataset part, the selected ESL training set is the same as [16]. The ordinary test images are the common datasets, Set5 [34] and Set14 [18]. The deep undercooling melt images are provided by National Space Science Center, Chinese Academy of Sciences.

In evaluation metrics, we selected widely used PSNR and SSIM data indices as the objective indicators. The PSNR value represents the weighted mean square error(WMSE) of each pixel between the reconstructed image and the corresponding original image. The larger the value, the more similar the two images are, and vice versa. The SSIM value represents the structural difference between the two images, which is a decimal from 0 to 1. The closer the value is to 1, the better the reconstruction effect, the closer the value is to 0, the more obvious the structural difference between the two images.

4.1 Parameter Settings

When we reconstruct an image based on the ISL, the size of the extracted patch is set to 3×3 pixels, and the size of the searched neighboring image patch changes with the magnification factor. For example, when the magnification factor is 2, the search patch size is 6×6 pixels, and when the magnification factor is 3, the search patch size is 9×9 pixels. In dictionary learning part, we also set the size of the extracted patch to 3×3 pixels. When the magnification factor is 2, the overlapping is 1, and when the magnification factor is 3, the overlapping is 2. The sparse threshold τ of representation coefficient is 3, and usually the weight λ is 1. The size of the HR dictionary D_x is 25×1024 , and the size of the LR dictionary D_y is 100×1024 . The weight φ is set to 1 when we reconstruct an image based on an ESL.

Preference parameters x , y , w and z for reconstructing images based on mixed sample library are set to 0.006, 0.994, 0.003, and 0.997, respectively. The parameter p in (11) is set to 1. And the parameter δ in Eq.(15) is also set to 1.

4.2 Result Analysis

In this section, the results are shown in ordinary images and deep undercooling melt these two parts respectively. Our method presents the superiority by contrasting with others.

Reconstruction contrast of ordinary images. Below we will compare the reconstructed images from objective indicators and subjective feelings. We first use Set5 and Set14 as test images, which are magnified 2x and 3x respectively. The corresponding PSNR (db) and SSIM indicators are shown in Table 1, Table 2. The bold represents the highest data and the italic represents the second highest data.

From Table 3, we can see that when the image is magnified 2x, compared to other methods, our algorithm index is in the second position behind KimSR, and takes the first place in some scenes (e.g., butterfly, bridge, man). At the same time, compared with AMSLSM, which we have not implemented LDMO algorithm, both PSNR and SSIM have been greatly improved. This fact also shows the optimization algorithm possess its own effectiveness.

Table 3. The PSNR (dB) and SSIM values of images for up-scaling $\times 2$ by using different SR methods (set5 and set14)

Image	Method															
	BIC		YangSR [15]		ZeydeSR [18]		TimofteSR [14]		HuangSR [32]		KimSR [33]		AMSLSM		AMS-LMDO	
	PSNR	SSIM	PSNR	SSIM	PSNR	SSIM	PSNR	SSIM	PSNR	SSIM	PSNR	SSIM	PSNR	SSIM	PSNR	SSIM
baby	37.12	0.9352	-	-	38.25	0.9628	38.52	0.9647	38.46	0.9643	38.75	0.9667	38.17	0.9604	<i>38.65</i>	<i>0.9649</i>
bird	36.85	0.9566	-	-	39.93	0.9836	41.12	<i>0.9865</i>	41.07	0.9864	42.42	0.9890	39.02	0.9773	<i>41.26</i>	0.9648
butterfly	27.43	0.9264	-	-	30.65	0.9541	32.01	0.9652	31.94	0.9635	<i>34.49</i>	<i>0.9750</i>	29.94	0.9437	34.51	0.9762
head	34.94	0.8542	-	-	35.59	0.8819	35.77	0.8867	35.68	0.8852	35.93	0.8900	35.51	0.8804	<i>35.90</i>	<i>0.8897</i>
woman	32.12	0.9457	-	-	34.49	0.9646	35.31	<i>0.9694</i>	35.36	0.9690	36.05	0.9730	33.87	0.9587	<i>35.41</i>	0.9657
Average1	33.69	0.9236	-	-	35.78	0.9494	36.55	<i>0.9545</i>	36.50	<i>0.9537</i>	37.53	0.9587	35.30	0.9441	<i>37.15</i>	0.9523
baboon	24.36	0.7277	-	-	25.47	0.7522	25.65	0.7662	25.52	0.7625	25.94	0.7787	25.37	0.7512	25.54	<i>0.7665</i>
barbara	26.59	0.8495	-	-	28.70	0.8707	28.70	0.8749	28.49	0.8742	28.41	<i>0.8777</i>	27.86	0.8675	28.55	0.8924
bridge	24.97	0.8126	-	-	27.55	0.8398	27.78	0.8498	25.89	0.8258	<i>28.05</i>	<i>0.8585</i>	27.08	0.8267	28.36	0.8595
coastguard	29.69	0.8175	-	-	30.41	0.8373	30.57	0.8428	30.70	<i>0.8473</i>	<i>30.99</i>	0.8549	30.30	0.8346	31.06	0.8456
comic	26.35	0.8695	-	-	27.65	0.8959	28.29	0.9110	28.35	0.9149	29.40	0.9319	27.56	0.8937	28.63	<i>0.9173</i>
face	33.37	0.8497	-	-	35.57	0.8820	35.74	0.8868	35.63	0.8851	35.91	0.8900	34.81	0.8728	<i>35.89</i>	<i>0.8899</i>
flowers	30.75	0.9001	-	-	32.28	0.9271	33.02	<i>0.9356</i>	33.02	0.9354	<i>34.33</i>	0.9459	32.04	0.9242	34.35	0.9341
foreman	33.67	0.9457	-	-	36.18	0.9687	36.94	<i>0.9727</i>	36.79	0.9689	37.40	0.9737	36.04	0.9633	<i>37.02</i>	0.9704
lenna	35.48	0.9023	-	-	36.21	0.9262	36.60	<i>0.9296</i>	36.52	0.9289	37.06	0.9326	36.11	0.9234	<i>36.71</i>	0.9284
man	28.96	0.8438	-	-	30.44	0.8770	30.87	0.8859	30.83	0.8851	<i>31.43</i>	<i>0.8963</i>	30.07	0.8739	31.55	0.8972
monarch	33.25	0.9585	-	-	35.75	0.9726	37.01	0.9767	37.22	0.9762	39.40	0.9809	34.93	0.9694	37.15	<i>0.9771</i>
pepper	35.74	0.8991	-	-	36.59	0.9188	37.02	<i>0.9216</i>	37.00	0.9211	<i>37.37</i>	0.9240	36.24	0.9143	37.39	0.9204
ppt3	27.68	0.9442	-	-	29.30	0.9694	30.09	0.9768	31.43	0.9821	32.81	0.9871	29.05	0.9587	30.14	<i>0.9834</i>
zebra	31.52	0.9161	-	-	33.21	0.9388	33.59	0.9426	33.79	0.9431	34.23	0.9456	32.94	0.9258	<i>34.20</i>	<i>0.9435</i>
Average2	30.17	0.8740	-	-	31.81	0.8983	32.28	0.9052	32.23	0.9036	33.05	0.9127	31.46	0.8928	<i>32.61</i>	<i>0.9090</i>

As can be seen from Table 4, when the image is zoomed in 3 times, our algorithm achieves the same results as Table 3 shows, and obtained first place in some scenes (e.g., woman, face, foreman). This illustrates the robust and reliability of our algorithm.

Table 4. The PSNR (dB) and SSIM values of images for up-scaling $\times 3$ by using different SR methods (set5 and set14)

Image	Method															
	BIC		YangSR [15]		ZeydeSR [18]		TimofteSR [14]		HuangSR [32]		KimSR [33]		AMSLSM		AMS-LMDO	
	PSNR	SSIM	PSNR	SSIM	PSNR	SSIM	PSNR	SSIM	PSNR	SSIM	PSNR	SSIM	PSNR	SSIM	PSNR	SSIM
baby	33.91	0.9039	34.29	0.9043	35.08	0.9202	35.21	0.9225	35.20	0.9236	35.38	0.9261	34.62	0.9157	35.38	0.9228
bird	32.57	0.9256	34.10	0.9391	34.57	0.9478	35.54	0.9560	35.76	0.9583	36.66	0.9643	34.38	0.9435	35.61	0.9585
butterfly	24.04	0.8216	25.58	0.8611	25.94	0.8803	27.24	0.9124	26.92	0.9060	29.96	0.9423	25.63	0.9076	28.95	0.9381
head	32.88	0.8003	33.17	0.8024	33.56	0.8197	33.77	0.8268	33.74	0.8272	33.96	0.8337	33.34	0.8068	33.94	0.8370
woman	28.56	0.8896	29.93	0.9037	30.37	0.9185	31.20	0.9296	31.45	0.9319	32.36	0.9404	30.08	0.9164	32.44	0.9404
Average1	30.39	0.8682	31.41	0.8821	31.90	0.8973	32.59	0.9095	32.61	0.9094	33.66	0.9214	31.61	0.8980	33.26	0.9194
baboon	23.21	0.5439	23.47	0.5878	23.52	0.5903	23.62	0.6070	23.53	0.6041	23.78	0.6205	23.50	0.5880	23.61	0.6036
barbara	26.25	0.7531	26.39	0.7633	26.76	0.7785	26.47	0.7759	26.96	0.7911	26.21	0.7805	26.54	0.7736	26.74	0.7837
bridge	24.40	0.6483	24.82	0.6920	25.02	0.6985	25.17	0.7113	24.08	0.6865	25.38	0.7238	24.95	0.6968	25.30	0.7145
coastguard	26.55	0.6149	27.01	0.6393	27.15	0.6499	27.27	0.6584	27.23	0.6608	27.35	0.6722	27.08	0.6472	27.29	0.6592
comic	23.12	0.6988	23.90	0.7557	23.96	0.7524	24.38	0.7771	24.41	0.7838	25.11	0.8121	23.93	0.7566	24.43	0.7826
face	32.82	0.7984	33.11	0.8011	33.53	0.8190	33.76	0.8268	33.71	0.8265	33.95	0.8330	33.24	0.8126	33.97	0.8467
flowers	27.23	0.8013	28.25	0.8297	28.43	0.8364	29.05	0.8516	29.10	0.8550	30.01	0.8720	28.37	0.8339	29.14	0.8533
foreman	31.16	0.9058	32.00	0.9129	33.19	0.9323	34.30	0.9428	34.22	0.9386	35.00	0.9484	32.82	0.9241	35.22	0.9485
lenna	31.68	0.8582	32.64	0.8648	33.00	0.8771	33.52	0.8842	33.51	0.8860	33.97	0.8911	32.94	0.8673	33.61	0.8853
man	27.01	0.7495	27.76	0.7749	27.90	0.7852	28.28	0.7987	28.34	0.8023	28.78	0.8151	27.87	0.7792	28.35	0.8002
monarch	29.43	0.9198	30.71	0.9290	31.10	0.9371	32.14	0.9463	32.10	0.9476	34.69	0.9601	30.95	0.9365	33.80	0.9573
pepper	32.38	0.8698	33.32	0.8668	34.07	0.8859	34.74	0.8914	34.82	0.8929	35.30	0.8969	33.62	0.8724	34.83	0.8926
ppt3	23.70	0.8746	24.98	0.8918	25.23	0.9087	26.09	0.9319	27.08	0.9481	27.86	0.9616	25.04	0.9004	27.57	0.9467
zebra	26.63	0.7942	27.95	0.8259	28.49	0.8421	28.98	0.8513	29.18	0.8527	29.50	0.8585	28.11	0.8362	29.07	0.8524
Average2	27.54	0.7736	28.31	0.7954	28.67	0.8067	29.13	0.8182	29.16	0.8197	29.78	0.8318	28.50	0.8018	29.50	0.8233

In order to reveal our algorithm more intuitively, we also give a comparison of reconstructed images, as shown in Fig. 3 and Fig. 4. Compared to interpolation-based or single-sample-library-based methods, our algorithm makes the beard in Fig. 3 clearer, and the flower texture in Fig. 4 more natural and realistic. This certifies that our algorithm can recover the image detail texture very well, which is significant for the deep undercooling melt reconstruction.

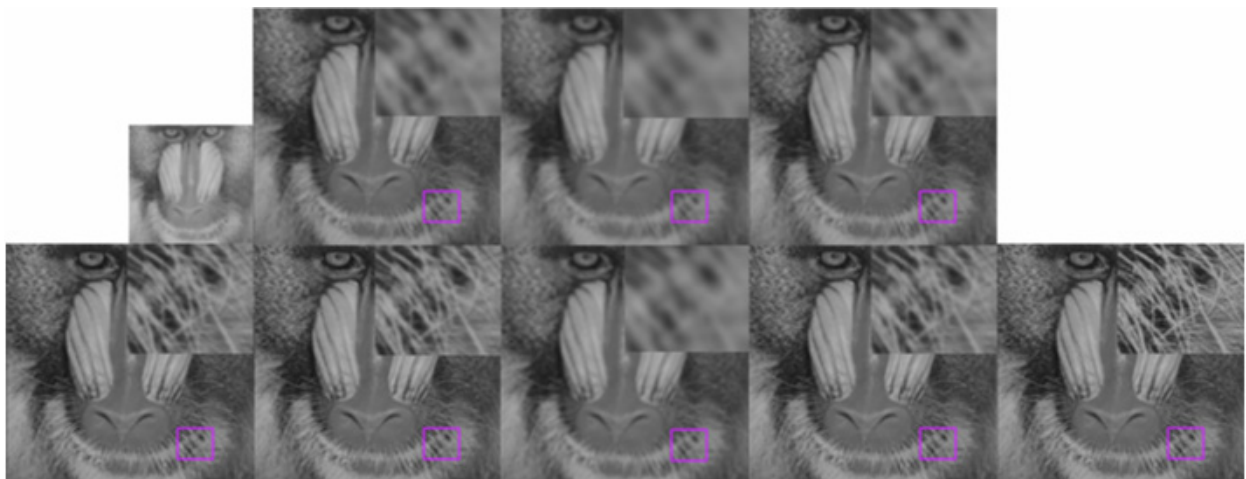


Fig. 3. 2 \times SR results of the 'baboon' image. Images from top to bottom and left to right: input image, reconstructed high resolution image by BIC, ZeydeSR, TimofteSR, HuangSR, KimSR, AMSLSM, and AMS-LMDO, as well as the original image

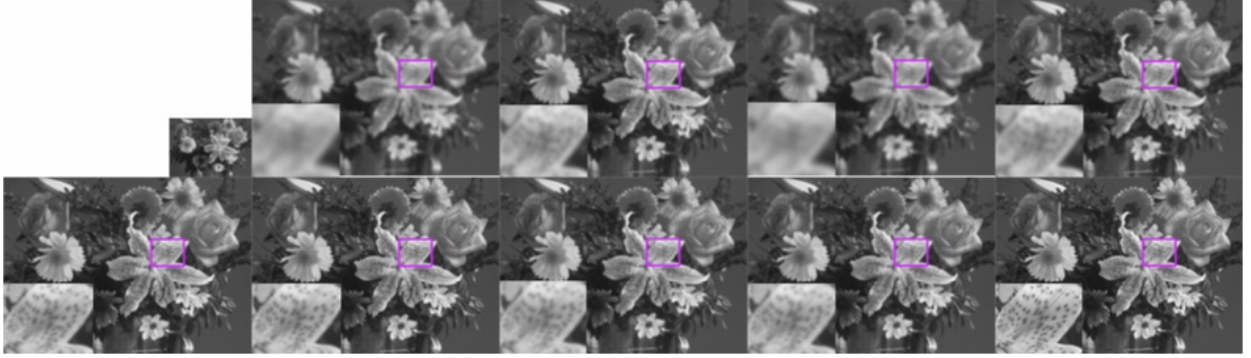


Fig. 4. $3\times$ SR results of the ‘flowers’ image. Images from top to bottom and left to right: input image, reconstructed high resolution image by BIC, YangSR, ZeydeSR, TimofteSR, HuangSR, KimSR, AMSLSM, and AMS-LMDO, as well as the original image

It is undoubtable that using neural networks to reconstruct images must cost expensive hardware and too much time, while our method can complete the task in less time on an ordinary personal computer. Although KimSR is a little better than our method, but considering the hardware and time-consuming factors, our approach still has much more advantages.

Reconstruction contrast of deep undercooling melt. The structure of this section is the same as the previous section. In this section, we reconstruct the deep undercooling melt image using the AMS-LMDO algorithm. The experimental results are shown in Table 5 and Table 6.

Table 5. The PSNR (dB) and SSIM values of images for up-scaling $\times 2$ by using different SR methods (deep undercooling melt)

Image	Method															
	BIC		YangSR [15]		ZeydeSR [18]		TimofteSR [14]		HuangSR [32]		KimSR [33]		AMSLSM		AMS-LMDO	
	PSNR	SSIM	PSNR	SSIM	PSNR	SSIM	PSNR	SSIM	PSNR	SSIM	PSNR	SSIM	PSNR	SSIM	PSNR	SSIM
melt1	36.34	0.8560	-	-	37.16	0.8961	37.35	0.9002	37.44	0.9015	37.98	0.9058	36.85	0.8894	38.56	0.9113
melt2	40.88	0.9646	-	-	46.38	0.9777	46.46	0.9779	46.53	0.9783	46.68	0.9787	43.59	0.9769	47.53	0.9881
Average	38.61	0.9103	-	-	41.77	0.9369	41.91	0.9391	41.99	0.9399	42.33	0.9423	40.22	0.9332	43.05	0.9497

Table 6. The PSNR (dB) and SSIM values of images for up-scaling $\times 3$ by using different SR methods (deep undercooling melt)

Image	Method															
	BIC		YangSR [15]		ZeydeSR [18]		TimofteSR [14]		HuangSR [32]		KimSR [33]		AMSLSM		AMS-LMDO	
	PSNR	SSIM	PSNR	SSIM	PSNR	SSIM	PSNR	SSIM	PSNR	SSIM	PSNR	SSIM	PSNR	SSIM	PSNR	SSIM
melt1	33.41	0.7853	33.86	0.7924	34.35	0.8727	34.42	0.8835	34.59	0.8874	34.84	0.9004	34.04	0.8531	35.56	0.8941
melt2	37.54	0.9498	37.71	0.9563	37.93	0.9575	38.57	0.9595	38.66	0.9605	38.82	0.9624	37.83	0.9569	39.74	0.9702
Average	35.48	0.8676	35.79	0.8744	36.14	0.9151	36.50	0.9215	36.63	0.9240	36.83	0.9314	35.94	0.9050	37.65	0.9322

From Table 5 and Table 6, we can see that the proposed algorithm has achieved the best results in both the $2\times$ magnification and the $3\times$ magnification. Compared with the second KimSR, our PSNR index increased by 0.72db and SSIM increased by 0.0074 when the melts $2\times$ magnified, and as the magnification turns into $3\times$, our PSNR index increased by 0.82db and SSIM increased by 0.0008. Furthermore, compared with proposed AMSLSM, after LMDO processing, the PSNR and SSIM were increased by 2.83db and 0.0165 respectively under the condition of $2\times$ magnified, and 1.71db, 0.0272 under the condition of $3\times$ magnified. To more intuitively illustrate the superiority of our algorithm in reconstructing deep undercooling melts, we plot Fig. 5 and Fig. 6. From the figures we can see that the AMS-LMDO algorithm maintains a relatively leading position on the common dataset, especially possesses the superior performance for the deep undercooling melts. The deep undercooling melts processed by our method is closer to the original image in the evaluation of objective indices.

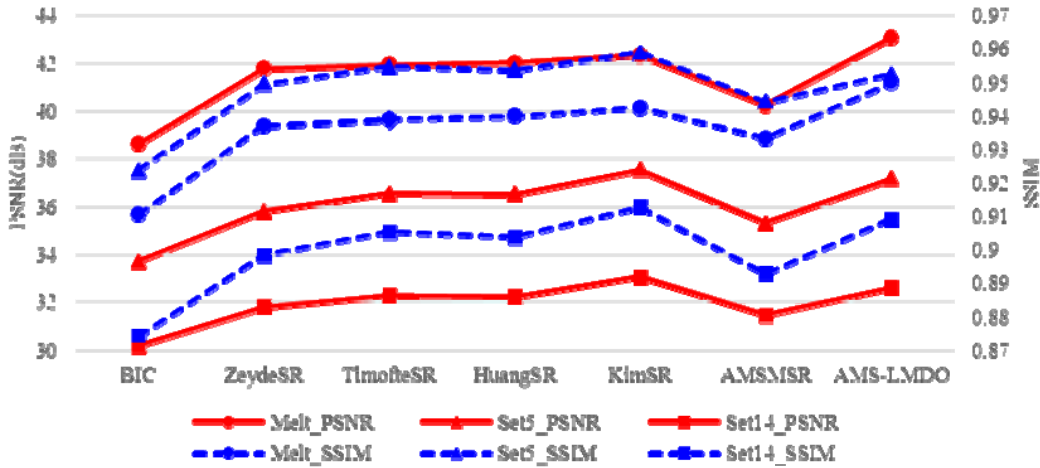


Fig. 5. Line chart after magnifying the image $\times 2$ using different method

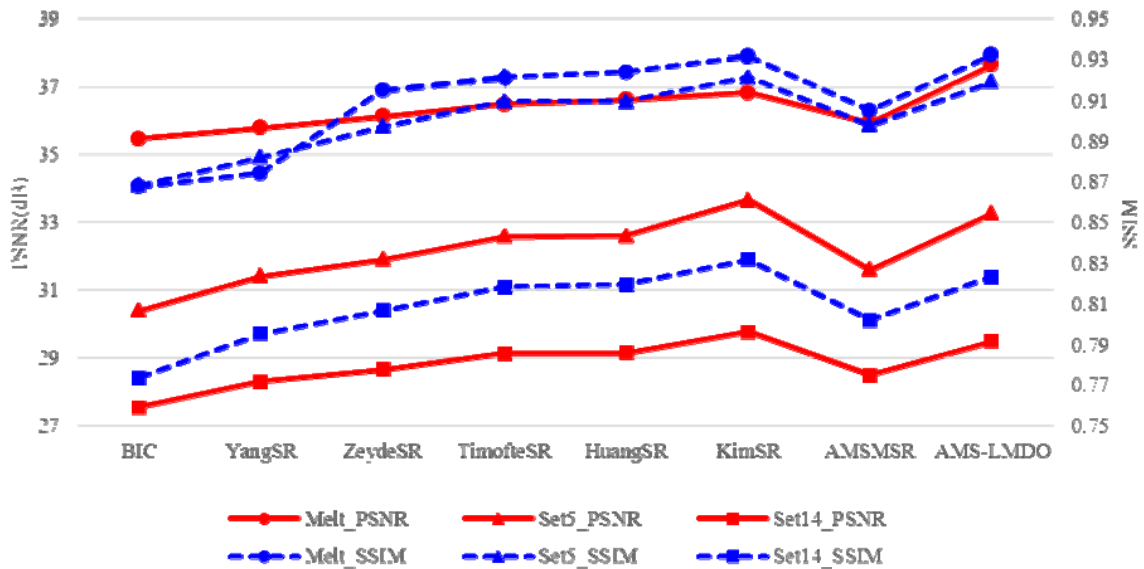


Fig. 6. Line chart after magnifying the image $\times 3$ using different methods

Fig. 7 and Fig. 8 show the results of reconstructing the deep undercooling melt using different algorithms. Take the image of $2\times$ magnified as an example: The experiment is consistent with previous experimental results. Our algorithm can recover the texture information of the deep undercooling melts very well, avoiding the occurrence of error-information-caused smoothing or blurring. There are sharper edges that make the reconstructed image closer to the original image. These are all of great significance for researchers to continue studying the relevant properties of deep undercooling melts and discovering new materials.

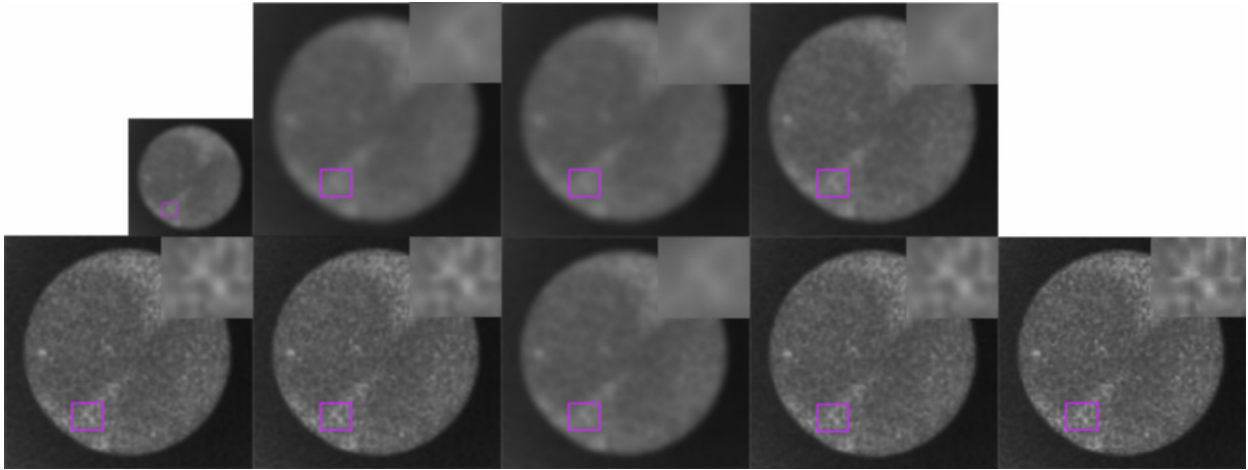


Fig. 7. $2\times$ SR results of the ‘melt2’ image. Images from top to bottom and left to right: input image, reconstructed high resolution image by BIC, ZeydeSR, TimofteSR, HuangSR, KimSR, AMSLSM, and AMS-LMDO, as well as the original image

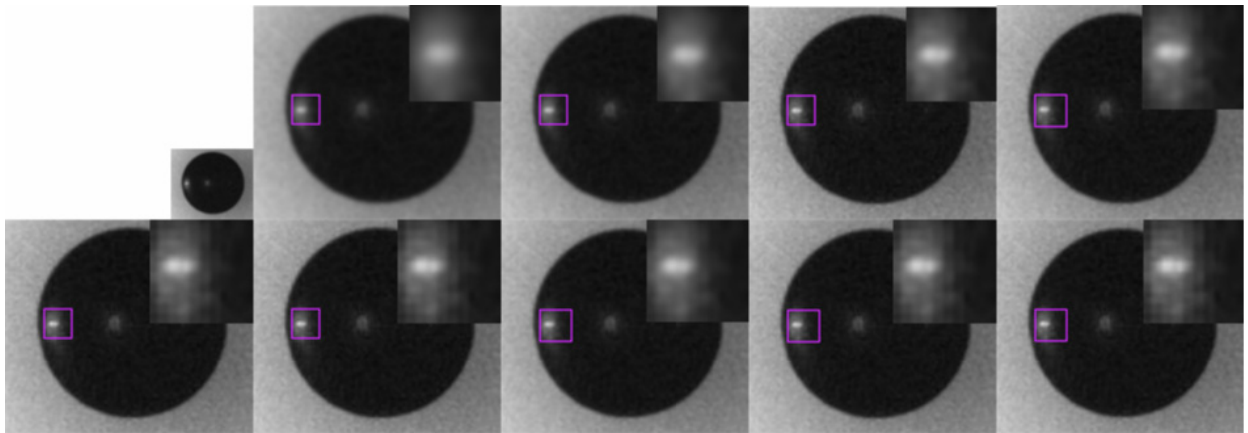


Fig. 8. $3\times$ SR results of the ‘melt1’ image. Images from top to bottom and left to right: input image, reconstructed high resolution image by BIC, YangSR, ZeydeSR, TimofteSR, HuangSR, KimSR, AMSLSM, and AMS-LMDO, as well as the original image

We believe that the proposed algorithm can be so advantageous because: (1) we built a mixed sample library and developed an adaptive selection algorithm, which help us to fully consider and balance the relationship between sparse coding and image self-similarity, especially when we process specific samples (e.g., deep undercooling melts); (2) We used the optimization algorithm LMDO for the reconstructed HR image to further remove the error information in the image.

5 Conclusion

This paper proposes an improved image SR method, combining the advantages of the internal sample library and the external sample library, so that the reconstructed image is closer to the real scene. The method overcomes the difficulty of insufficient information provided by internal sample library and inaccurate information provided by external sample library, and integrates different types of prior information provided by the mixed sample library, thereby improving the accuracy of image reconstruction. After the reconstruction, the low-rank matrix decomposition is used to remove the error information in HR images to further enhance the reconstruction effect. Simulation results show that the proposed method is suitable for reconstruction of many types of images. Especially when reconstructing deep undercooling melt images, our AMS-LMDO method not only reconstructs more detail textures, but also preserves sharp edges compared to current popular methods. This is very important for the study of

deep undercooling melts. Next, we will optimize the algorithm to further improve the reconstruction effect and reduce the time complexity.

Acknowledgments

This work was partially supported by a grant from the National Natural Science Foundation of China (No. 61573019). Research of bionic polarization/optical flow/INS integrated navigation based on the probability distribution optical flow estimation.

References

- [1] J. Gao, T. Volkman, J. Strohmenger, D.M. Herlach, Phase selection in undercooled Nd-Fe-Co-B alloy droplets, *Materials Science and Engineering: A* 375(2004) 498-501.
- [2] X.-H. Luo, L. Chen, Investigation of microgravity effect on solidification of medium-low-melting-point alloy by drop tube experiment, *Science in China Series E: Technological Sciences* 51(9)(2008) 1370-1379.
- [3] K.Y. Kamal, R. Herranz, J.J.W.A. van Loon, P.C.M. Christianen, F.J. Medina, Evaluation of simulated microgravity environments induced by diamagnetic levitation of plant cell suspension Cultures, *Microgravity Science and Technology* 28(3)(2016) 309-317.
- [4] Z. Zou, X. Luo, Q. Yu, Droplet image super resolution based on sparse representation and kernel regression, *Microgravity Science and Technology* 30(3)(2018) 321-329.
- [5] N. Akhtar, F. Shafait, A. Mian, Hierarchical beta process with Gaussian process prior for hyperspectral image super resolution, in: *Proc. European Conference on Computer Vision*, 2016.
- [6] J. Sun, J. Sun, Z. Xu, H.-Y. Shum, Gradient profile prior and its applications in image super-resolution and enhancement, *IEEE Transactions on Image Processing* 20(6)(2010) 1529-1542.
- [7] K.V. Mishra, M. Cho, A. Kruger, W. Xu, Spectral super-resolution with prior knowledge, *IEEE transactions on signal processing* 63(20)(2015) 5342-5357.
- [8] Y. Chen, Y. Tai, X. Liu, C. Shen, J. Yang, Fsrnet: End-to-end learning face super-resolution with facial priors, in: *Proc. 2018 IEEE Conference on Computer Vision and Pattern Recognition*, 2018
- [9] J.A. Tropp, A.C. Gilbert, Signal recovery from random measurements via orthogonal matching pursuit, *IEEE Transactions on information theory* 53(12)(2007) 4655-4666.
- [10] D. Glasner, S. Bagon, M. Irani, Super-resolution from a single image, in: *Proc. IEEE 12th International Conference on Computer Vision*, 2009.
- [11] M. Zontak, M. Irani, Internal statistics of a single natural image, in: *Proc. 2011 IEEE Conference on Computer Vision and Pattern Recognition*, 2011.
- [12] I. Mosseri, M. Zontak, M. Irani, Combining the power of internal and external denoising, in: *Proc. IEEE International Conference on Computational Photography*, 2013.
- [13] W.T. Freeman, T.R. Jones, E.C. Pasztor, Example-based super-resolution, *IEEE Computer Graphics and Applications* 22(2)(2002)56-65.
- [14] H. Zhang, Y. Zhang, H. Li, T.-S. Huang, Generative Bayesian image super resolution with natural image prior, *IEEE Transactions on Image Processing* 21(9)(2012) 4054-4067.

- [15] J. Yang, J. Wright, T.-S. Huang, Y. Ma, Image super-resolution via sparse representation, *IEEE Transactions on Image Processing* 19(11)(2010) 2861-2873.
- [16] J. Yang, J. Wright, T. Huang, Y. Ma, Image super-resolution as sparse representation of raw image patches, in: *Proc. 2008 IEEE Conference on Computer Vision and Pattern Recognition*, 2008.
- [17] S. Wang, L. Zhang, Y. Liang, Q. Pan, Semi-coupled dictionary learning with applications to image super-resolution and photo-sketch synthesis, in: *Proc. 2012 IEEE Conference on Computer Vision and Pattern Recognition*, 2012.
- [18] R. Zeyde, M. Elad, M. Protter, On single image scale-up using sparse-representations, in: *Proc. International Conference on Curves and Surfaces*, 2010.
- [19] W. Dong, L. Zhang, R. Lukac, G. Shi, Sparse representation based image interpolation with nonlocal autoregressive modeling, *IEEE Transactions on Image Processing* 22(4)(2013) 1382-1394.
- [20] W. Dong, L. Zhang, G. Shi, X. Wu, Image deblurring and super-resolution by adaptive sparse domain selection and adaptive regularization, *IEEE Transactions on Image Processing* 20(7)(2011) 1838-1857.
- [21] R. Timofte, V. De, L.V. Gool, Anchored neighborhood regression for fast example-based super-resolution, in: *Proc. 2013 IEEE International Conference on Computer Vision*, 2013.
- [22] R. Timofte, V. De Smet, L. Van Gool, A plus: adjusted anchored neighborhood regression for fast super-resolution, in: *Proc. Asian Conference on Computer Vision*, 2014.
- [23] Z. Zhu, F. Guo, H. Yu, C. Chen, Fast single image super-resolution via self-example learning and sparse representation, *IEEE Transactions on Multimedia* 16(8)(2014) 2178-2190.
- [24] C.-Y. Yang, J.B. Huang, M.-H. Yang, Exploiting self-similarities for single frame super-resolution, in: *Proc. Asian Conference on Computer vision*, 2010.
- [25] Z. Wang, Y. Yang, Z. Wang, S. Chang, J. Yang, T.-S. Huang, Learning super-resolution jointly from external and internal examples, *IEEE Transactions on Image Processing* 24(11)(2015) 4359-4371.
- [26] S. Wang, B. Yue, X. Liang, L. Jiao, How does the low-rank matrix decomposition help internal and external learning for super-resolution, *IEEE Transactions on Image Processing* 27(3)(2018) 1086-1099.
- [27] A. Buades, B. Coll, J. Morel, A non-local algorithm for image denoising, in: *Proc. 2005 IEEE Computer Society Conference on Computer Vision and Pattern Recognition*, 2005.
- [28] M. Aharon, M. Elad, A. Bruckstein, K-SVD: an algorithm for designing overcomplete dictionaries for sparse representation, *IEEE Transactions on signal processing* 54(11)(2006) 4311-4322.
- [29] J. Yang, Z. Wang, Z. Lin, S. Cohen, T. Huang, Coupled dictionary training for image super-resolution, *IEEE Transactions on Image Processing* 21(8)(2012) 3467-3478.
- [30] J. Zhang, D. Zhao, W. Gao, Group-based sparse representation for image restoration, *IEEE Transactions on Image Processing* 23(8)(2014) 3336-3351.
- [31] R. Rubinstein, M. Zibulevsky, M. Elad, Efficient implementation of the K-SVD algorithm using batch orthogonal matching pursuit, *CS Technion report CS-2008-08*, 2008.
- [32] J. Huang, A. Singh, N. Ahuja, Single image super-resolution from transformed self-exemplars, in: *Proc. 2015 IEEE Conference on Computer Vision and Pattern Recognition*, 2015.
- [33] J. Kim, J. K. Lee, K. M. Lee, Accurate image super-resolution using very deep convolutional networks, in: *Proc. 2016 IEEE Conference on Computer Vision and Pattern Recognition*, 2016.

- [34] M. Bevilacqua, A. Roumy, C. Guillemot, M.-L.A. Morel, Low-complexity single-image super-resolution based on nonnegative neighbor embedding, in: Proc. British Machine Vision Conference, 2012.